Uncertainty Quantification of Human Electromagnetic Exposure from Mobile Phone Antenna Based on Migration-CoKriging

Shenghang Huo[1], Yujia Song[2*], Alistair Duffy[3], *Fellow*, *IEEE*, and Jinjun Bai[1]

Abstract—**The safety of mobile phone antennas concerning electromagnetic exposure to the human body has become a prominent research focus in recent years. Uncertainties in antenna design and manufacturing processes may result in actual electromagnetic radiation levels deviating from design standards, thereby posing a potential risk of electromagnetic exposure. Finite element simulation has emerged as a crucial tool for predicting the specific absorption rate (SAR), owing to its capability to accurately model complex structures. The effective integration of finite element simulation with uncertainty quantification provides valuable scientific insights for optimizing design, shortening research and development cycles, and minimizing commissioning costs. This article proposes an uncertainty quantification method based on Migration-CoKriging (MCK). This method solves the limitations of traditional Co-Kriging that cannot be achieved without a low-precision solver by calculating cross-domain correlations. A more accurate surrogate model is constructed using a smaller training set, which improves the core performance of uncertainty quantification. MCK is combined with Sobol and applied in sensitivity analysis to quantify the influence of each random variable on SAR, thereby establishing a rigorous theoretical foundation for mobile phone antenna design and electromagnetic radiation safety.**

Index Terms—**Electromagnetic exposure, mobile phone antenna, Migration-CoKriging (MCK), specific absorption rate (SAR), sensitivity analysis, uncertainty quantification**

I. INTRODUCTION

Mobile phones have become an integral part of daily life. However, their internal antennas can expose users to electromagnetic radiation. Mobile phones are often held near the user's head, particularly during calls. With growing public awareness of health concerns, the potential effects of mobile phone electromagnetic radiation have garnered significant attention [1].

To safeguard mobile phone users from potentially harmful electromagnetic radiation, the specific absorption rate (SAR) serves as a quantitative measure of the electromagnetic power

absorbed per unit mass of biological tissue. The International Commission on Non-Ionizing Radiation Protection (ICNIRP) [2] and the Institute of Electrical and Electronics Engineers (IEEE) [3] have established safety thresholds for SAR levels. Jamshed et al. [4] investigated a dual-antenna mobile phone system and integrated multiple mechanisms, including relative phase adjustment, coupled control, and power distribution, to collaboratively reduce SAR. Liang et al. [5] introduced a strategy to achieve uniform current distribution in a single direction and developed a mobile phone antenna with high head-hand efficiency and low SAR. The measurement of SAR using standard dosimetric facilities is both costly and time-consuming during the antenna design process [6]. Consequently, finite element simulation has emerged as an efficient and viable alternative for modeling human electromagnetic exposure. However, uncertainties exist in the design and manufacturing of antennas, including factors such as manufacturing tolerances and material aging [7], [8]. Incorporating uncertainty quantification into antenna design is essential for several reasons: First, simulation models typically rely on idealized assumptions, which can result in discrepancies between simulated and actual test results. Second, the consistency of antenna product quality is a critical factor influencing its real-world performance. Third, conventional SAR assessment methods primarily rely on fixed models and single parameters, limiting their ability to accurately capture electromagnetic exposure in complex environments. Integrating uncertainty quantification with finite element simulation enables a more comprehensive assessment and serves as a scientific foundation for establishing electromagnetic exposure standards.

The Monte Carlo method (MCM) is widely regarded as the most reliable approach for uncertainty quantification due to its high accuracy [9]. However, its computational inefficiency renders it impractical for uncertainty quantification in finite element simulations with high time costs [10]. Several efficient uncertainty quantification methods have been proposed, among which polynomial chaos expansion (PCE) [11], Kriging [12], and support vector regression (SVR) [13] are the most widely adopted. Enhancing their performance in uncertainty quantification has been a focal research topic over the past decade, leading to the development of numerous high-performance algorithms. Blatman et al. [14] propose a sparse PCE method based on least-angle regression (LAR) to

reduce the computational cost of high-dimensional uncertainty finite element simulations. Leifsson et al. [15] combine the global prediction of PCE with the local interpolation of Kriging to propose the polynomial chaos Kriging (PCK) method, which is applied to the yield estimation of antennas. In addition, the performance of SVR and least squares support vector regression (LSSVR) is not affected by the dimension of the input data, and they are used to quantify the uncertainty of high-dimensional inputs [16], [17].

These methods fundamentally function as surrogate models, meaning they approximate system behavior by analyzing the relationship between uncertain input parameters and system response [18]. Although advanced surrogate models such as PCE-LAR, PCK, and LSSVR have demonstrated strong performance in addressing specific problems, they all face an inherent limitation: the accuracy of uncertainty quantification improves with the availability of more training data. However, obtaining sufficient training data necessitates conducting numerous finite element simulations, which incurs substantial computational costs.

To overcome this limitation in surrogate modeling, an uncertainty quantification method based on Co-Kriging has been proposed [19]. This approach enhances the efficiency and accuracy of surrogate models by integrating useful information from extensive low-precision data with a limited amount of high-precision data. The implementation of Co-Kriging requires two solvers that represent the same physical model: a high-precision solver with substantial computational cost (e.g., finite element simulation) and a low-precision solver with reduced computational expense (e.g., approximate formula methods). However, for complex electromagnetic simulation models (e.g., SAR analysis of human exposure to electromagnetic fields from mobile phone antennas), suitable low-precision solvers are often unavailable. As a result, the applicability of Co-Kriging is constrained, rendering it unsuitable for uncertainty quantification in complex electromagnetic systems.

This article proposes an enhanced algorithm, termed Migration-CoKriging (MCK), designed to overcome the constraint that traditional Co-Kriging requires the availability of a low-precision solver. The methodological framework is structured as follows.

1) A simplified model is developed from the high-precision finite element simulation model to generate low-precision simulation data. Unlike the low-precision solver in traditional Co-Kriging, the simplified model does not maintain complete physical consistency with the original model.

2) A mapping function is employed to project the input parameters of both high-precision and low-precision models onto a shared feature space.

3) Cross-domain correlation is calculated in the feature space via cross-covariance. The low-precision data derived from the simplified model is integrated with high-precision data to develop an accurate surrogate model with significantly reduced computational cost.

This article considers the impact of uncertainty factors in the design and manufacturing process of mobile phone antennas on human electromagnetic exposure. The MCK method is employed to quantify the uncertainty in the specific absorption rate (SAR) of a planar inverted-F antenna (PIFA) when positioned for a typical mobile phone call. Based on the MCK model, the Sobol index is estimated using the exhaustive sampling method to calculate the global sensitivity index of all random variables in the PIFA human electromagnetic radiation system.

The structure of this paper is outlined as follows. Section II presents the fundamental principles of traditional Co-Kriging and the proposed MCK methodology. Section III establishes the PIFA model, SAM model, and a simplified model, along with relevant exposure scenarios, and applies MCK to quantify the uncertainty in human head SAR. Section IV analyzes how variations in both the quality and quantity of low-precision samples influence the performance of MCK. Section V integrates MCK with Sobol indices to conduct a global sensitivity analysis. Section VI summarizes this paper.

II. METHODOLOGY

Uncertainty quantification is a systematic approach for quantitatively assessing how input uncertainties propagate to affect the output. Uncertainty factors are typically represented by a random variable model in vector form, expressed as

$$\boldsymbol{\xi} = \left\{ \xi_1, \xi_2, ..., \xi_j, ..., \xi_m \right\} \qquad (1)$$

where ξ_i is a random variable, $\boldsymbol{\xi}$ is a vector of random variables, and m is the number of random variables.

The initial step in surrogate-model-based uncertainty quantification is to generate the sample set $\boldsymbol{S}_h = \left[\boldsymbol{x}_1^h, \boldsymbol{x}_2^h, \cdots, \boldsymbol{x}_N^h \right]$. The random variable vector $\boldsymbol{\xi}$ is characterized by the sample set $\boldsymbol{S}_h$. Here, the number of sample points is N, and each sample point $\boldsymbol{x}_i^h$ is represented as a m-dimensional vector, denoted as

$$\boldsymbol{x}_i^h = \left\{ x_i^h(1), x_i^h(2), ..., x_i^h(j), ..., x_i^h(m) \right\} \qquad (2)$$

where $x_i^h(j)$ are constant values, corresponding to ξ_j in (1). Deterministic electromagnetic simulation is performed on $\boldsymbol{S}_h$, as in

$$\boldsymbol{y}_i^h = \text{EM}[\boldsymbol{x}_i^h] \qquad (3)$$

where $\text{EM}[\bullet]$ represents a single deterministic electromagnetic simulation process, $\boldsymbol{y}_i^h$ is an interesting output. $\boldsymbol{Y}^h = \left[\boldsymbol{y}_1^h, \boldsymbol{y}_2^h, \cdots, \boldsymbol{y}_N^h \right]^{\text{T}}$ is the set of response values. Finally, the surrogate model is constructed based on the training set $\{\boldsymbol{x}_i^h, \boldsymbol{y}_i^h\}_{i=1}^N$. In general, the larger the number of sample points N, the more accurate the surrogate model. However, obtaining a sufficient number of training points in finite element electromagnetic simulation is expensive.

A. Co-Kriging

The high-precision training set used in Co-Kriging denoted as

$\{\boldsymbol{x}_i^h, \boldsymbol{y}_i^h\}_{i=1}^N$, serves as the basis for constructing traditional surrogate models. It is typically derived from high-precision yet computationally expensive finite-element electromagnetic simulations. The low-precision training set, denoted as $\{\boldsymbol{x}_j^l, \boldsymbol{y}_j^l\}_{j=1}^n$, is computed over a large number of sample points $\boldsymbol{S}_l = \left[\boldsymbol{x}_1^l, \boldsymbol{x}_2^l, \cdots, \boldsymbol{x}_n^l\right]$ using a low-precision solver (e.g., an approximate formula method) with minimal computational cost. Here, $\boldsymbol{Y}^l = \left[\boldsymbol{y}_1^l, \boldsymbol{y}_2^l, \cdots, \boldsymbol{y}_n^l\right]^{\mathrm{T}}$ represents the set of response values, and $n > N$.

The predicted value of the Co-Kriging model is defined as

$$\hat{Y}(\boldsymbol{x}) = \boldsymbol{\lambda}_1^{\mathrm{T}} \boldsymbol{Y}^h + \boldsymbol{\lambda}_2^{\mathrm{T}} \boldsymbol{Y}^l \tag{4}$$

where $\boldsymbol{\lambda}_1$ and $\boldsymbol{\lambda}_2$ represent the weighting factors for the high-precision and low-precision response values, respectively. The response value at any given point is obtained by solving for $\boldsymbol{\lambda}_1$ and $\boldsymbol{\lambda}_2$. Statistical assumptions are introduced to determine these weighting factors. $\boldsymbol{Y}^h$ and $\boldsymbol{Y}^l$ are replaced by a random process, as

$$\begin{cases} Y_1(\boldsymbol{x}) = \beta_1 + Z_1(\boldsymbol{x}) \\ Y_2(\boldsymbol{x}) = \beta_2 + Z_2(\boldsymbol{x}) \end{cases} \tag{5}$$

where β_1 and β_2 are constant mean. $Z_1(\bullet)$ and $Z_2(\bullet)$ are zero mean stationary random processes. The covariance and cross-covariance are defined as

$$\boldsymbol{C}^{(11)} = \mathrm{Cov}[Z_1(\boldsymbol{x}), Z_1(\boldsymbol{x}')] = \sigma_1^2 R^{(11)}(\boldsymbol{x}, \boldsymbol{x}')$$
$$\boldsymbol{C}^{(12)} = \mathrm{Cov}[Z_1(\boldsymbol{x}), Z_2(\boldsymbol{x}')] = \sigma_1 \sigma_2 R^{(12)}(\boldsymbol{x}, \boldsymbol{x}') \tag{6}$$
$$\boldsymbol{C}^{(22)} = \mathrm{Cov}[Z_2(\boldsymbol{x}), Z_2(\boldsymbol{x}')] = \sigma_2^2 R^{(22)}(\boldsymbol{x}, \boldsymbol{x}')$$

where σ_1^2 and σ_2^2 are the process variances of the random processes $Y_1(\boldsymbol{x})$ and $Y_2(\boldsymbol{x})$, respectively. $R^{(11)}$ and $R^{(22)}$ correspond to the spatial correlation functions of the high-precision and low-precision data, respectively, while $R^{(12)}$ represents the cross-correlation function.

The weight factors $\boldsymbol{\lambda}_1$ and $\boldsymbol{\lambda}_2$ can be obtained from the Co-Kriging equation set, as follows

$$\begin{bmatrix} \boldsymbol{C}^{(11)} & \boldsymbol{C}^{(12)} & \mathbf{1} & \mathbf{0} \\ \boldsymbol{C}^{(21)} & \boldsymbol{C}^{(22)} & \mathbf{0} & \mathbf{1} \\ \mathbf{1}^{\mathrm{T}} & \mathbf{0}^{\mathrm{T}} & 0 & 0 \\ \mathbf{0}^{\mathrm{T}} & \mathbf{1}^{\mathrm{T}} & 0 & 0 \end{bmatrix} \begin{bmatrix} \boldsymbol{\lambda}_1 \\ \boldsymbol{\lambda}_2 \\ \mu_1/2 \\ \mu_2/2 \end{bmatrix} = \begin{bmatrix} \boldsymbol{c}_1(\boldsymbol{x}) \\ \boldsymbol{c}_2(\boldsymbol{x}) \\ 1 \\ 0 \end{bmatrix} \tag{7}$$

where $\boldsymbol{\mu} = \{\mu_1, \mu_2\}^{\mathrm{T}}$ is the Lagrangian multiplier vector. $\boldsymbol{c}_1$ and $\boldsymbol{c}_2$ are the target point covariance vectors.

The essence of Co-Kriging is to jointly construct the spatial correlation of high-precision and low-precision data through a structured covariance matrix. The self-covariance terms, $\boldsymbol{C}^{(11)}$ and $\boldsymbol{C}^{(22)}$, describe the spatial continuity within their respective datasets, while the cross-covariance term, $\boldsymbol{C}^{(12)}$, quantifies the correlation strength between high-precision and low-precision data. This enables low-precision data to supplement the physical phenomena not covered by the

high-precision model through correction terms.

However, the implementation of traditional Co-Kriging faces two key limitations. First, for some complex electromagnetic systems, no corresponding low-precision solver exists, making Co-Kriging infeasible. Second, Co-Kriging requires the high-precision and low-precision models to be identical in physical description (e.g., shape and size) to ensure effective data integration.

B. Migration-CoKriging

The MCK proposed in this article enables users to construct simplified models by modifying shape or size to reduce computational complexity, where the original model serves as a homology-heteromorphic reference. Instead of using Euclidean distance in the traditional physical parameter space, MCK employs a cross-domain correlation computation method. This overcomes the limitation of traditional Co-Kriging, which cannot be implemented without a low-precision solver.

In traditional Co-Kriging, the cross-covariance $\boldsymbol{C}^{(12)}$ depends on the proximity of high-precision and low-precision models in the physical parameter space. However, homology-heteromorphic models cannot be directly aligned. Fig. 1. shows the block diagram of the MCK model. The inputs $\boldsymbol{S}_h = \left[\boldsymbol{x}_1^h, \boldsymbol{x}_2^h, \cdots, \boldsymbol{x}_N^h\right]$ of the high-precision model and $\boldsymbol{S}_l = \left[\boldsymbol{x}_1^l, \boldsymbol{x}_2^l, \cdots, \boldsymbol{x}_n^l\right]$ of the low-precision model are mapped to the feature space $\mathcal{Z}$ via the mapping functions ϕ_h and ϕ_l, as

$$\begin{cases} \phi_h : \boldsymbol{x}^h \to \mathcal{Z} \\ \phi_l : \boldsymbol{x}^l \to \mathcal{Z} \end{cases} \tag{8}$$

make high-precision and low-precision data comparable in feature space.

Minimize the distribution difference between high-precision and low-precision data in the feature space, as

$$\begin{aligned} \mathcal{L}_{\mathrm{MMD}} &= \left\| \frac{1}{N} \sum_{i=1}^N \phi_h(\boldsymbol{x}_i^h) - \frac{1}{n} \sum_{j=1}^n \phi_l(\boldsymbol{x}_j^l) \right\|_{\mathcal{H}}^2 \\ &= \frac{1}{N^2} \sum_{i=1}^N \sum_{j=1}^N K(\phi_h(\boldsymbol{x}_i^h), \phi_h(\boldsymbol{x}_j^h)) \\ &+ \frac{1}{n^2} \sum_{i=1}^n \sum_{j=1}^n K(\phi_l(\boldsymbol{x}_i^l), \phi_l(\boldsymbol{x}_j^l)) \\ &- \frac{2}{Nn} \sum_{i=1}^N \sum_{j=1}^n K(\phi_h(\boldsymbol{x}_i^h), \phi_l(\boldsymbol{x}_j^l)) \end{aligned} \tag{9}$$

where $\mathcal{H}$ is the reproducing kernel Hilbert space.

Constraints are introduced, as

$$\mathcal{L}_{\mathrm{reg}} = \beta(\| \phi_h \|^2 + \| \phi_l \|^2) \tag{10}$$

to constrain the complexity of the mapping functions ϕ_h and ϕ_l to avoid overfitting.

In order to solve the weight coefficients $\boldsymbol{\lambda}_1$ and $\boldsymbol{\lambda}_2$ of MCK, the total objective function is minimized as

$$\mathcal{L} = \mathcal{L}_{\mathrm{CoKriging}} + \alpha \mathcal{L}_{\mathrm{MMD}} + \mathcal{L}_{\mathrm{reg}} \tag{11}$$

where $\mathcal{L}_{\mathrm{CoKriging}}$ is the prediction error term, as in
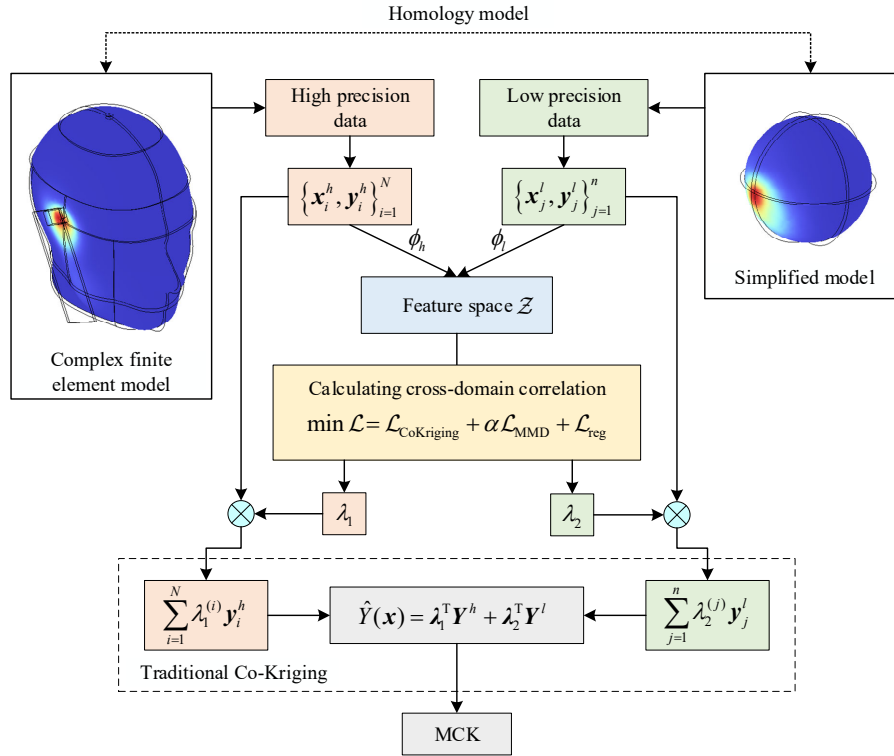
Fig. 1. Construction of the MCK model.

$$\mathcal{L}_{\text{CoKriging}} = \frac{1}{N}\sum_{i=1}^{N}\left(Y_1(\boldsymbol{x}_i^h) - \hat{Y}_{\text{MCK}}(\boldsymbol{x}_i^h)\right)^2$$
$$+ \frac{1}{n}\sum_{j=1}^{n}\left(\rho Y_2(\boldsymbol{x}_j^l) - \hat{Y}_{\text{MCK}}(\boldsymbol{x}_j^l)\right)^2 \tag{12}$$

where ρ is the scaling factor.

Cross-domain correlations are calculated in the feature space, replacing the Euclidean distance in the traditional physical parameter space. The covariance matrix of MCK is obtained as

$$\boldsymbol{C} = \begin{bmatrix} \boldsymbol{C}_{hh} & \boldsymbol{C}_{hl} \\ \boldsymbol{C}_{lh} & \boldsymbol{C}_{ll} \end{bmatrix} \tag{13}$$

where the self-correlation matrix and the cross-correlation matrix transform to

$$\begin{cases} \boldsymbol{C}_{hh} = K_h(\phi_h(\boldsymbol{x}_i^h), \phi_h(\boldsymbol{x}_j^h)) \\ \quad = \sigma_h^2 \exp\left(-\sum_{p=1}^{k}\frac{(\phi_h^{(p)}(\boldsymbol{x}_i^h) - \phi_h^{(p)}(\boldsymbol{x}_j^h))^2}{\theta_p}\right) \\ \boldsymbol{C}_{ll} = K_l(\phi_l(\boldsymbol{x}_i^l), \phi_l(\boldsymbol{x}_j^l)) \\ \quad = \sigma_l^2 \exp\left(-\sum_{p=1}^{k}\frac{(\phi_l^{(p)}(\boldsymbol{x}_i^l) - \phi_l^{(p)}(\boldsymbol{x}_j^l))^2}{\theta_p}\right) \\ \boldsymbol{C}_{hl} = K_{hl}(\phi_h(\boldsymbol{x}_i^h), \phi_l(\boldsymbol{x}_j^l)) \\ \quad = \sigma_h\sigma_l \exp\left(-\sum_{p=1}^{k}\frac{(\phi_h^{(p)}(\boldsymbol{x}_i^h) - \phi_l^{(p)}(\boldsymbol{x}_j^l))^2}{\theta_p}\right) \end{cases} \tag{14}$$

where θ_p represents the length-scale parameter for each dimension of the feature space, while $\phi_h^{(p)}$ and $\phi_l^{(p)}$ denote the components in the pth dimension of the feature space.

Based on the reconstructed covariance matrix, the weight coefficients λ_1 and λ_2 are solved by traditional Co-Kriging to obtain the MCK model as in

$$\hat{Y}_{\text{MCK}}(\boldsymbol{x}) = M_{\text{MCK}}(\boldsymbol{x}) = \lambda_1^{\text{T}}\boldsymbol{Y}^h + \lambda_2^{\text{T}}\boldsymbol{Y}^l. \tag{15}$$

C. Global Sensitivity Analysis

Global sensitivity analysis is a fundamental application of uncertainty quantification, with Sobol index-based sensitivity analysis being one of the most widely used and well-established methods [20], [21]. Identifying key input variables that significantly influence human electromagnetic exposure through sensitivity analysis provides a crucial theoretical foundation for antenna design, manufacturing, and electromagnetic safety protection. This article proposes a sensitivity analysis framework based on the MCK model that combines the exhaustive sampling method to estimate the Sobol index. The aim is to ensure accuracy while efficiently calculating the global sensitivity index of different variables.

The Sobol method is founded on the principle of variance decomposition, which partitions the total variance of the model output into contributions from individual input variables (first-order effects) and variances arising from interactions between multiple variables (higher-order effects). The original model is expressed as a sum of incremental terms, as follows

$$Y(\boldsymbol{x}) = y_0 + \sum_{i=1}^{m}y_i(x_i) + \sum_{1<i<j<m}y_{ij}(x_i, x_j)$$
$$+ ... + y_{1,2,...,m}(x_1,...,x_m) \tag{16}$$

where y_0 is the average value of $Y(\boldsymbol{x})$.

(16) is orthogonal, and the variance of the model response can be expanded as
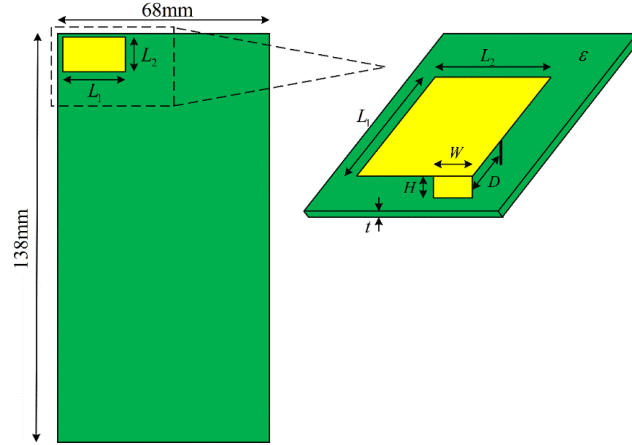
Fig. 2. Schematic diagram of PIFA.

TABLE I
RANDOM VARIABLES MODELING FOR PIFA

Uniform random variables		U [min, max]	Unit
Length of radiant sheet	L_1	U [21.8, 22.2]	mm
Width of radiant sheet	L_2	U [9.8, 10.2]	mm
Antenna height	H	U [3.9, 4.1]	mm
Width of shorting piece	W	U [2.4, 2.6]	mm
Distance from feed point to shorting pin	D	U [3.15, 3.35]	mm
Substrate thickness	t	U [1.45, 1.55]	mm
Substrate dielectric constant	ε	U [4.45, 4.55]	/

$$Var[Y] = D = \sum_{i=1}^{m} D_i + \sum_{1 \le i < j \le m} D_{ij} + \cdots + D_{1,2,\ldots,m} . \quad (17)$$

The Sobol index is defined as

$$S_{i_1,\ldots,i_s} = \frac{D_{i_1,\ldots,i_s}}{D}, 1 \le i_1 < \ldots < i_s \le m . \quad (18)$$

The first-order Sobol index, S_i, measures the influence of individual input variables, whereas the higher-order Sobol index, $S_{i_1,\ldots,i_s}$, quantifies the effects of interactions among multiple variables. The total Sobol index, S_i^T, for an input variable x_i, is computed as the sum of all Sobol indices associated with this variable:

$$S_i^T = \sum_{\{i_1,\ldots,i_s\} \supset i} S_{i_1,\ldots,i_s} . \quad (19)$$

Sobol indices are computed using the constructed MCK model, as follows:

$$\begin{cases} \hat{y}_0 = \frac{1}{\theta} \sum_{\vartheta=1}^{\theta} M_{\text{MCK}}(\boldsymbol{x}^{(\vartheta)}) \\ \hat{D} = \frac{1}{\theta} \sum_{\vartheta=1}^{\theta} M_{\text{MCK}}^2(\boldsymbol{x}^{(\vartheta)}) - \hat{y}_0^2 \\ \hat{D}_i = \frac{1}{\theta} \sum_{\vartheta=1}^{\theta} M_{\text{MCK}}(x_i^{(\vartheta)}, \boldsymbol{x}_{\sim i}^{(\vartheta)}) M_{\text{MCK}}(x_i^{(\vartheta)}, \boldsymbol{x}_{\sim i}'^{(\vartheta)}) - \hat{y}_0^2 \end{cases} \quad (20)$$

where θ is the number of exhaustive sampling points. $\boldsymbol{x}_{\sim i}^{(\vartheta)}$ is
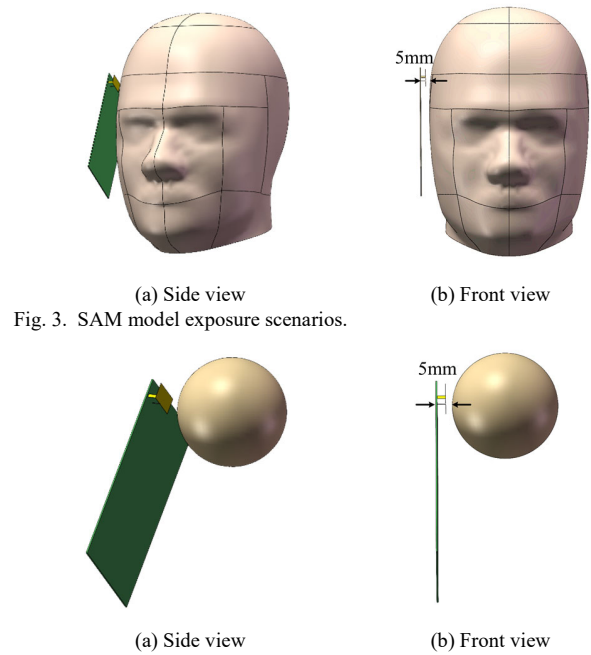
(a) Side view   (b) Front view
Fig. 3. SAM model exposure scenarios.
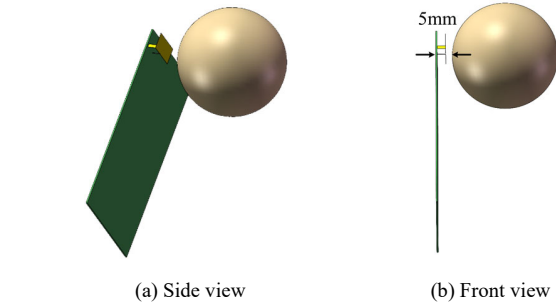

(a) Side view   (b) Front view
Fig. 4. Simplified model exposure scenarios.

the observed value excluding the ith input variable. $\boldsymbol{x}'$ represents the realization of x independent of $\{x_i^{(\vartheta)}, \boldsymbol{x}_{\sim i}^{(\vartheta)}\}$.

III. UNCERTAINTY QUANTIFICATION OF SAR FOR THE HUMAN HEAD EXPOSED TO PIFA ELECTROMAGNETIC FIELDS

In this section, the uncertainty quantification of SAR in a human head exposed to the PIFA electromagnetic field is conducted, and the proposed MCK method is compared with four classical uncertainty quantification methods: Kriging, LSSVR, PCE-LAR, and PCK.

A. Simulation Model Construction

The PIFA used in this study is shown in Fig. 2 and is positioned at the upper-left corner of the substrate. Based on the dimensions of a typical smartphone, the substrate is set to a length of 138 mm and a width of 68 mm. The uncertainty modeling of the substrate's thickness and dielectric constant, along with the relevant parameters of the PIFA, is presented in
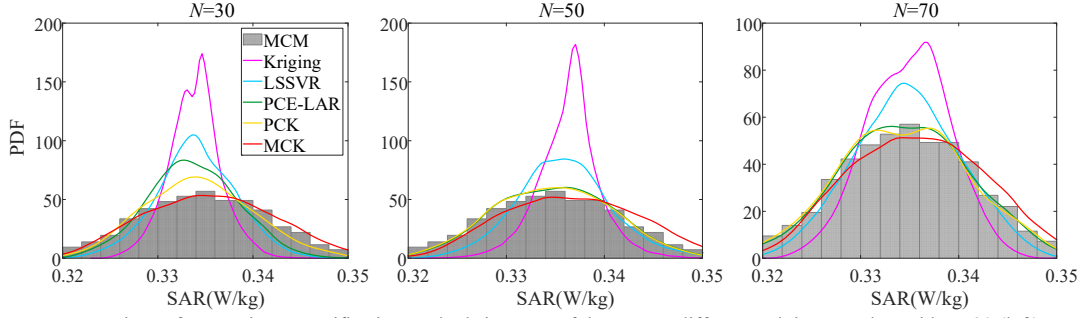
Fig. 5. PDF of SAR. Comparison of uncertainty quantification methods in terms of the PDF at different training samples, with N=30 (left), N=50 (middle), and N=70 (right) samples. It is worth noting that all MCMs are identical, with differences in the range of axes leading to visual differences.

TABLE II
DIELECTRIC PROPERTIES OF SAM AT 2.45 GHz

	Dielectric constant	Conductivity (S/m)
Internal tissue	39.2	1.8
Shell	3.7	0.008

Table I, assuming a uniform distribution of the variables.

The construction of MCK requires both high-precision and low-precision simulation data. A specific anthropomorphic mannequin (SAM) [22], [23], shown in Fig. 3, is used as a high-precision model to evaluate head exposure. The SAM consists of internal tissues and an outer shell with a thickness of 2 mm. According to IEEE recommendations [23], the default mobile phone call position is depicted in Fig. 3. The distance between the substrate and the human head is set to 5 mm, aligning with industry standards.

A simplified model, serving as a low-precision model, is shown in Fig. 4. A spherical model with significantly smaller sizes than the SAM is constructed to reduce computational costs. The simplified model is identical to the SAM except for its size and shape. It also consists of internal tissues and a shell with a thickness of 2 mm, positioned 5 mm from the phone substrate. The center of the substrate's top (corresponding to the earpiece) aligns in a straight line with the center of the sphere in the simplified model.

This article investigates the uncertainty quantification of SAR in the human head when exposed to the PIFA electromagnetic field at a frequency of 2.45 GHz. SAR at a specific point in human tissue (also known as local SAR) [24], [25] is defined as

$$SAR = \frac{\sigma |\mathbf{E}|^2}{2\rho} \tag{21}$$

where, σ represents the electrical conductivity of body tissue, ρ denotes the mass density, and $\mathbf{E}$ is the electric field vector. The dielectric properties of SAM at 2.45 GHz [23], [26] are listed in Table II. Notably, the SAR limit specified in radio frequency exposure standards refers not to local SAR but to peak spatial average SAR [3], [5], [27], which represents the maximum average SAR within any 1 g or 10 g of tissue in a cubic volume. The spatial average SAR is defined as

$$SAR_V = \frac{1}{V} \int_V \frac{\sigma |\mathbf{E}(\mathbf{r})|^2}{2\rho} dv. \tag{22}$$

TABLE III
MEAM VALUE

	N=30	N=50	N=70
Kriging	0.3941	0.4507	0.6088
LSSVR	0.6000	0.6929	0.7791
PCE-LAR	0.6942	0.8514	0.9108
PCK	0.8282	0.8558	0.9292
MCK	0.9719	0.9223	0.9580

MCM serves as the reference data for comparing the MEAM values of various uncertainty quantification methods across different training sample sizes.

TABLE IV
RELATIVE ERROR

	N=30		N=50		N=70	
	δ_μ	δ_σ	δ_μ	δ_σ	δ_μ	δ_σ
Kriging	0.31%	60.59%	0.44%	54.93%	0.01%	39.12%
LSSVR	0.27%	40.00%	0.28%	30.71%	0.05%	22.09%
PCE-LAR	0.37%	30.58%	0.01%	14.86%	0.10%	8.92%
PCK	0.21%	17.18%	0.04%	14.42%	0.15%	7.08%
MCK	0.19%	0.45%	0.55%	0.36%	0.29%	0.40%

Relative errors in the means and standard deviations of each uncertainty quantification method compared to MCM (δ_μ and δ_σ).

This study focuses on the maximum average SAR in 1 g of tissue for uncertainty quantification. To validate the effectiveness of the proposed method, MCM with 2,000 simulations is used as the reference standard to compare the accuracy and computational cost of various uncertainty quantification methods. The low-precision data $\{\mathbf{x}_j^l, \mathbf{y}_j^l\}_{j=1}^n$ for MCK is generated by performing 300 simulations on a simplified model with a radius of 3 cm. The high-precision data denoted as $\{\mathbf{x}_i^h, \mathbf{y}_i^h\}_{i=1}^N$, corresponds to the same training set used to construct other surrogate models.

B. Comparison of Different Uncertainty Quantification Methods

Fig. 5 presents the probability density function (PDF) of SAR obtained from three different training sets. The results indicate that the MCK model trained with 30 high-precision
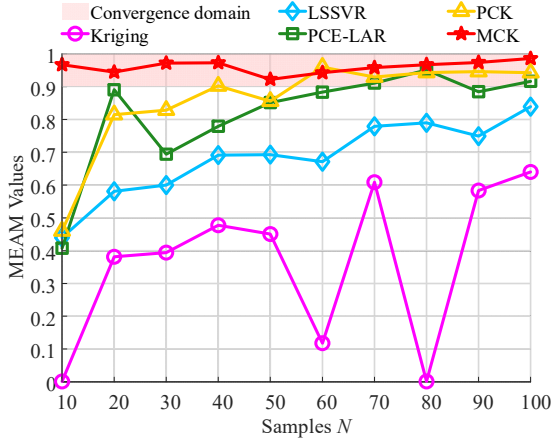
Fig. 6. Convergence of the MEAM value. Convergence domains refer to regions where the MEAM value exceeds the 0.9 threshold.

Fig. 7. PDF of SAR. Comparison of the PDF when the uncertainty quantification methods converge.

TABLE V
SIMULATION TIME

	t_H	t_L	t_M	t_{UQ}
PCE-LAR(N=70)	18.41h	/	5.43s	18.41h
PCK(N=60)	15.78h	/	6.71s	15.78h
MCK(N=10)	2.63h	1.25h	12.76s	3.88h

Comparing the computational costs of three converged uncertainty quantification methods. Kriging and LSSVR do not need to be compared because they do not converge for $N = 100$.

TABLE VI
NINE SITUATIONS FOR MCK

MCK	n=100	n=300	n=500
R=2cm	MCK-11	MCK-12	MCK-13
R=2.5cm	MCK-21	MCK-22	MCK-23
R=3cm	MCK-31	MCK-32	MCK-33

samples is very accurate and does not differ substantially from the MCK using 70 training samples. Both models closely align with the MCM reference. In contrast, PCE-LAR and PCK achieve comparable accuracy only when using the largest training set ($N = 70$), while Kriging and LSSVR demonstrate significantly lower accuracy, even with the maximum number of training samples.

To quantify the difference between the PDF of each uncertainty quantification method and the reference data, the mean equivalent area method (MEAM) [28] is employed. The MEAM evaluation result is a constant ranging from 0 to 1. A value closer to 1 indicates a smaller difference and a more accurate uncertainty quantification method. Table III presents the MEAM evaluation results for each uncertainty quantification method shown in Fig. 5. The MEAM values align with the trends observed in Fig. 5. MCK demonstrates high accuracy, achieving an MEAM value of 0.9719 at $N = 30$. In contrast, PCE-LAR and PCK exceed the 0.9 thresholds and attain high accuracy only at $N = 70$. The MEAM values for Kriging and LSSVR remain low even at the maximum training sample size, failing to meet accuracy requirements.

To validate the effectiveness of MEAM, the relative errors in the mean (δ_μ) and standard deviation (δ_σ) of each uncertainty quantification method, relative to MCM, are calculated, as shown in Table IV. The relative error of the mean is so small that it cannot be used as a criterion for determination. However, the standard deviation provides a very significant indication of the accuracy of each method. The relative error of the standard deviation is consistent with the results of the MEAM evaluation.
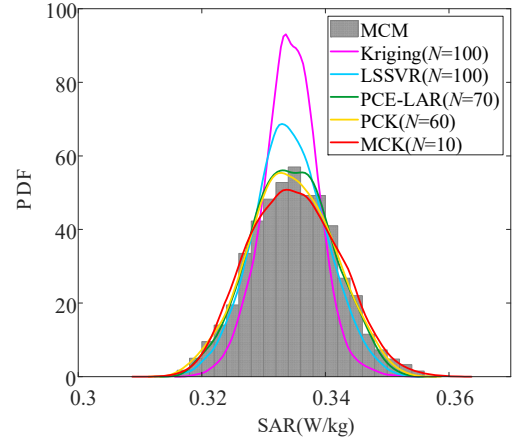
To further determine the sample size required for each uncertainty quantification method to achieve high accuracy, this study applies MEAM to assess convergence, as shown in Fig. 6. Convergence is defined as the minimum number of samples needed for the MEAM value to consistently remain above the 0.9 threshold. PCE-LAR and PCK converge within 70 and 60 samples, respectively, whereas Kriging and LSSVR fail to converge within 100 samples. In contrast, the MCK proposed in this article achieves convergence with only 10 samples.

Fig. 7 illustrates the PDF of all methods at convergence. The converged PCE-LAR and PCK closely approximate the MCM. In contrast, Kriging and LSSVR exhibit lower accuracy as they fail to converge even at the maximum sample size. The accuracy of Kriging is even much lower than that of LSSVR, which is due to the fact that Kriging is not suitable for dealing with high-dimensional complex nonlinear problems. Notably, MCK achieves accuracy comparable to MCM with the fewest high-precision samples.

Naturally, MCK's significantly faster convergence speed compared to other methods is closely linked to the incorporation of low-precision samples. Although low-precision simulation incurs some computational cost, it is minimal compared to that of high-precision simulation. Table V compares the computational time of MCK with that of the converged PCE-LAR and PCK. A single finite element simulation of the high-precision SAM model takes 15.78 minutes, resulting in a total computational time of 526 hours for 2,000 MCM simulations. PCE-LAR requires $t_H = 18.41$ h for 70 simulations, while PCK takes 15.78 hours for 60 simulations. In contrast, MCK completes 10 simulations in just 2.63 hours.

This article has been accepted for publication in IEEE Transactions on Antennas and Propagation. This is the author's version which has not been fully edited and content may change prior to final publication. Citation information: DOI 10.1109/TAP.2025.3590080

> REPLACE THIS LINE WITH YOUR PAPER IDENTIFICATION NUMBER (DOUBLE-CLICK HERE TO EDIT) <   8
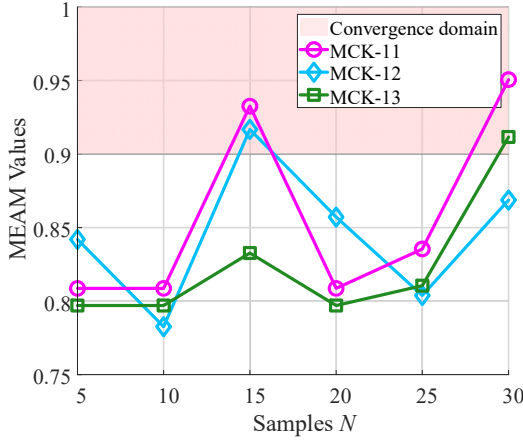
Fig. 8. Convergence of the MEAM value. Three cases of the simplified model with a radius of 2 cm are examined, each with a different number of low-precision data points.
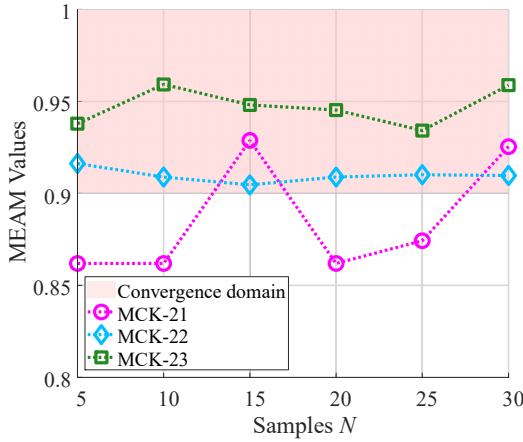

Fig. 9. Convergence of the MEAM value. Three cases of the simplified model with a radius of 2.5 cm are examined, each with a different number of low-precision data points.
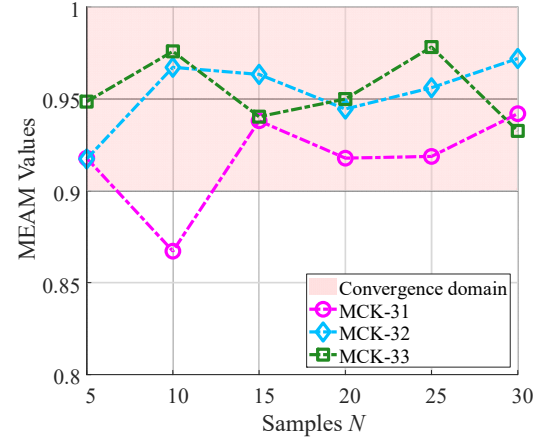

Fig. 10. Convergence of the MEAM value. Three cases of the simplified model with a radius of 3 cm are examined, each with a different number of low-precision data points.

TABLE VII
K-S DISTANCE AND COMPUTATIONAL COST OF THE 9-GROUP MCK

	D_{MCK}	t_H	t_L	t_{UQ}
MCK-11	0.021	7.89h	11.67min	8.08h
MCK-12	0.051	7.89h	35min	8.47h
MCK-13	0.029	7.89h	58.33min	8.86h
MCK-21	0.017	7.89h	16.67min	8.17h
MCK-22	0.019	1.315h	50min	2.15h
MCK-23	0.011	1.315h	83.33min	2.70h
MCK-31	0.014	3.945h	25min	4.36h
MCK-32	0.028	1.315h	75min	2.57h
MCK-33	0.025	1.315h	125min	3.40h

A single finite element simulation of the simplified sphere model takes 15 seconds, and the time t_L for MCK to perform 300 low-precision simulations is 1.25 hours. Compared to the finite element simulation time, the model prediction time t_M is negligible. Therefore, the total computation time t_{UQ} of MCK is 3.88 hours, demonstrating a significantly higher computational efficiency than PCE-LAR and PCK.

IV. DISCUSSION OF THE SIMPLIFIED DEGREE

The previous section demonstrated MCK's high accuracy and low computational cost by comparing several uncertainty quantification methods. However, MCK's performance depends on the quality of low-precision samples. Simplified models with smaller radii reduce computational costs. A key question is to what extent the simplified model's radius can be reduced while maintaining MCK's performance.

This section discusses the impact of low-precision sample quality (i.e., the radius of the simplified model) and quantity on MCK. Table VI lists the nine cases under analysis.

Figs. 8-10 present the convergence diagrams for the simplified model with three different radii. The smaller the simplified model, the lower the computational cost. Therefore,

models with smaller radii are preferred. As illustrated in Fig. 8, when the radius of the simplified model is 2 cm, MCK-11, MCK-12, and MCK-13 fail to converge before $N = 30$. MCK-11 and MCK-13 reach the convergence threshold at $N = 30$ and are likely to converge at this point. MCK-12 fails to reach the convergence threshold at $N = 30$. This indicates that an excessively small simplified model negatively affects both the accuracy and convergence speed of MCK. Furthermore, in this scenario, the impact of the number of low-precision data points (n) on the result is minimal.

Fig. 9 illustrates three cases of the simplified model with a radius of 2.5 cm: MCK-21, MCK-22, and MCK-23. As the number of low-precision samples increases, the convergence speed and accuracy of MCK improve significantly. The convergence speed of MCK-21 is slower than that of MCK-22 and MCK-23. Although MCK-22 and MCK-23 converge at the same speed ($N = 5$), the accuracy of MCK-22 is lower than that of MCK-23. Fig. 10 presents the case where the radius of the simplified model is 3 cm. MCK-32 and MCK-33 converge at $N = 5$ with similar accuracy. MCK-31 converges at $N = 15$. Therefore, when the simplified model is properly sized and the number of low-precision samples is sufficient, MCK exhibits fast convergence and high accuracy.

TABLE VIII
COMPUTATIONAL COST OF THE TWO SENSITIVITY ANALYSIS METHODS

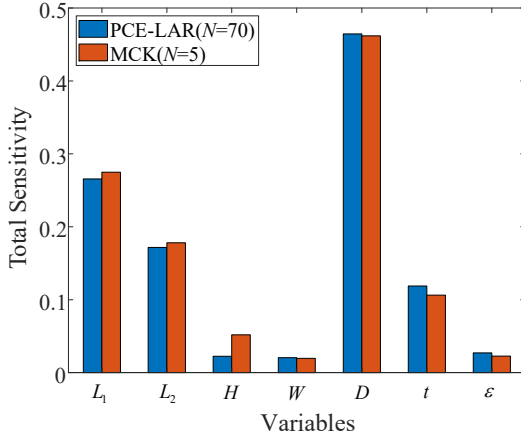|	t_{UQ}	t_P	t_S
PCE-LAR(N=70)	18.41h	/	18.41h
MCK(N=5)	2.15h	2.5min	2.19h

Fig. 11. Total sensitivity index. Comparison of total sensitivity indices for relevant variables in SAR uncertainty quantification under PIFA electromagnetic field exposure.

The accuracy of the 9-group MCK at convergence is further evaluated using the K-S distance, which serves as the test statistic for the Kolmogorov-Smirnov (K-S) test [29], [30]. The statistic D_{MCK} is determined by the maximum vertical deviation between the two curves of the cumulative distribution function (CDF) of the data set as

$$D_{MCK} = \max \left(\left| CDF_{MCM}(x) - CDF_{MCK}(x) \right| \right). \quad (23)$$

Table VII shows the K-S distance D_{MCK} and the time required for convergence of the nine MCK groups (the few cases where convergence is not reached are calculated based on $N = 30$). MCK-11, MCK-12, MCK-13, and MCK-21 are all calculated based on $N = 30$. The K-S distances of the 9 cases show the same results as Figs. 8-10. Except for MCK-12, D_{MCK} is less than 0.03 for all other cases. The single simulation time for the simplified model with a radius of 2 cm is 7 s. The single simulation time for a radius of 2.5 cm is 10 s. MCK-22, MCK-23, MCK-32, and MCK-33 all converge at $N = 5$ with a low time cost t_{UQ}. Among these, MCK-22 has the lowest computational cost, but its accuracy is slightly lower than that of MCK-23.

MCK integrates low-precision data from simplified models into high-precision data, ensuring both accuracy and computational efficiency. However, the radius of the simplified model cannot be reduced indefinitely. If the radius is too small, the simplified model's structure will deviate significantly from the SAM model, preventing the mapping function from effectively aligning the feature space. An insufficient number of low-precision samples can result in an inaccurate covariance matrix estimation, which in turn affects the calculation of the weight coefficients. This is consistent with the characteristics of traditional Co-Kriging.

Based on the results presented in this section, when the radius of the simplified model is set to 2 cm, the performance of MCK is inferior to that of simplified models with radii of 2.5 cm and 3 cm. This suggests that, for the scenario presented in this study, the optimal radius of the simplified model may lie at or between 2.5 cm and 2 cm. Further research is required to generalize the acceptable lower bound of model complexity.

V. SENSITIVITY ANALYSIS

The MCK-based sensitivity analysis method proposed in this article quantifies the impact of each PIFA input variable on head SAR and is compared with the PCE-LAR-based sensitivity analysis method. The MCK-based sensitivity analysis estimates the Sobol index using an exhaustive sampling method applied to the constructed MCK. Among the nine cases discussed in the previous section, MCK-22, which has the lowest computational cost, is selected. The number θ of exhaustive sampling points is 10^5, and the estimated computation cost t_P for the Sobol index is 2.5 min. The PCE-LAR-based sensitivity analysis method calculates the Sobol index directly from its coefficients without additional computational cost. However, its model construction cost t_{UQ} is significantly higher than that of MCK. Table VIII compares the computational costs of the two sensitivity analysis methods, showing that MCK is more efficient than PCE-LAR.

Fig. 11 presents the total sensitivity index of each variable. The results of both sensitivity analysis methods are largely consistent. The most influential variable on the SAR of the human head is the distance D from the feed point to the short-circuit pin. Additionally, the radiation sheet length L_1, width L_2, and substrate thickness t also have significant impacts. D, L_1, L_2 and t are identified as highly sensitive variables. Considering the safety of human electromagnetic exposure, the configuration of D, L_1, L_2 and t can be mainly considered in the design stage of the PIFA.

VI. CONCLUSION

This article proposes an MCK-based uncertainty quantification method for evaluating the SAR of the human head exposed to PIFA electromagnetic fields. A key advantage of this approach is that it overcomes the typical surrogate model limitation where accuracy strictly depends on the amount of training data. Additionally, it eliminates the reliance of traditional Co-Kriging on the consistency of high-precision and low-precision solver descriptions, significantly enhancing MCK's applicability. Compared to other methods, MCK has significant advantages in terms of accuracy and computational cost. The influence of both the quality and quantity of low-precision samples on MCK performance is discussed, and the applicability of the law of minimum cost is summarized to guide the subsequent use of MCK. Finally, MCK is combined with Sobol indices for sensitivity analysis to quantify the impact of each random variable on SAR, providing valuable insights for PIFA design.

REFERENCES

[1] H. H. Zhang, G. G. Yu, Y. Liu, Y. X. Fang, G. Shi, and S. Wang, "Design of Low-SAR Mobile Phone Antenna: Theory and Applications," *IEEE Trans. Antennas Propag.*, vol. 69, no. 2, pp. 698–707, Feb. 2021.

[2] M. H. Repacholi et al., "Health issues related to the use of hand-held radiotelephones and base transmitters. International Commission on Non-Ionizing Radiation Protection.," *Health physics*, vol. 70 4, pp. 587–93, 1996.

[3] *IEEE Standard for Safety Levels with Respect to Human Exposure to Radio Frequency Electromagnetic Fields, 3 kHz to 300 GHz*, IEEE Std C95.1-2005, Apr. 2006.

[4] M. A. Jamshed, T. W. C. Brown, and F. Héliot, "Dual Antenna Coupling Manipulation for Low SAR Smartphone Terminals in Talk Position," *IEEE Trans. Antennas Propag.*, vol. 70, no. 6, pp. 4299–4306, Jun. 2022.

[5] M. Yi Liang et al., "High Head–Hand Efficiency and Low-SAR Mobile Phone Antenna Design Based on Unidirectional and Uniform Current Distribution," *IEEE Trans. Antennas Propag.*, vol. 72, no. 7, pp. 5560–5568, Jul. 2024.

[6] M.-C. Gosselin, A. Christ, S. KÜhn, and N. Kuster, "Dependence of the Occupational Exposure to Mobile Phone Base Stations on the Properties of the Antenna and the Human Body," *IEEE Trans. Electromagn. Compat.*, vol. 51, no. 2, pp. 227–235, May 2009.

[7] D. Klink, P. Meyer, and W. Steyn, "Efficient Yield Estimation of Multiband Patch Antennas Using NLPLS-Based PCE," *IEEE Trans. Antennas Propag.*, vol. 70, no. 8, pp. 7037–7045, Aug. 2022.

[8] X. Cheng and V. Monebhurrun, "Application of Different Methods to Quantify Uncertainty in Specific Absorption Rate Calculation Using a CAD-Based Mobile Phone Model," *IEEE Trans. Electromagn. Compat.*, vol. 59, no. 1, pp. 14–23, Feb. 2017.

[9] R. Hu, V. Monebhurrun, R. Himeno, H. Yokota, and F. Costen, "A Statistical Parsimony Method for Uncertainty Quantification of FDTD Computation Based on the PCA and Ridge Regression," *IEEE Trans. Antennas Propag.*, vol. 67, no. 7, pp. 4726–4737, Jul. 2019.

[10] C. Salis and T. Zygiridis, "Dimensionality Reduction of the Polynomial Chaos Technique Based on the Method of Moments," *IEEE Antennas and Wireless Propagation Letters*, vol. 17, no. 12, pp. 2349–2353, 2018.

[11] D. Xiu and G. E. Karniadakis, "The Wiener--Askey Polynomial Chaos for Stochastic Differential Equations," *SIAM J. Sci. Comput.*, vol. 24, no. 2, pp. 619–644, Jan. 2002.

[12] R. Dwight and Z.-H. Han, "Efficient Uncertainty Quantification Using Gradient-Enhanced Kriging," in *50th AIAA/ASME/ASCE/AHS/ASC Structures, Structural Dynamics, and Materials Conference, Palm Springs, California: American Institute of Aeronautics and Astronautics*, May 2009.

[13] V. Cherkassky and Y. Ma, "Practical selection of SVM parameters and noise estimation for SVM regression," *Neural Networks*, vol. 17, no. 1, pp. 113–126, Jan. 2004.

[14] G. Blatman and B. Sudret, "Adaptive sparse polynomial chaos expansion based on least angle regression," *Journal of Computational Physics*, vol. 230, no. 6, pp. 2345–2367, Mar. 2011.

[15] L. Leifsson, X. Du, and S. Koziel, "Efficient yield estimation of multiband patch antennas by polynomial chaos-based Kriging," *International Journal of Numerical Modelling: Electronic Networks, Devices and Fields*, vol. 33, no. 6, p. e2722, 2020.

[16] R. Trinchero and F. G. Canavero, "Combining LS-SVM and GP Regression for the Uncertainty Quantification of the EMI of Power Converters Affected by Several Uncertain Parameters," *IEEE Trans. Electromagn. Compat.*, vol. 62, no. 5, pp. 1755–1762, Oct. 2020.

[17] R. Trinchero, M. Larbi, H. M. Torun, F. G. Canavero, and M. Swaminathan, "Machine Learning and Uncertainty Quantification for Surrogate Models of Integrated Devices With a Large Number of Parameters," *IEEE Access*, vol. 7, pp. 4056–4066, 2019.

[18] R. Hu, V. Monebhurrun, R. Himeno, H. Yokota, and F. Costen, "A General Framework for Building Surrogate Models for Uncertainty Quantification in Computational Electromagnetics," *IEEE Trans. Antennas Propag.*, vol. 70, no. 2, pp. 1402–1414, Feb. 2022.

[19] J. Bai, S. Huo, A. Duffy, and B. Hu, "Improvement of Nonembedded EMC Uncertainty Analysis Methods Based on Data Fusion Technique," *IEEE Trans. Electromagn. Compat.*, vol. 66, no. 6, pp. 1999–2009, Dec. 2024.

[20] B. Sudret, "Global sensitivity analysis using polynomial chaos expansions," *Reliability Engineering & System Safety*, vol. 93, no. 7, pp. 964–979, Jul. 2008.

[21] M. Ehre, I. Papaioannou, and D. Straub, "Global sensitivity analysis in high dimensions with PLS-PCE," *Reliability Engineering & System Safety*, vol. 198, p. 106861, Jun. 2020.

[22] *IEC/IEEE International Standard - Measurement procedure for the assessment of specific absorption rate of human exposure to radio frequency fields from hand-held and body-mounted wireless communication devices – Part 1528: Human models, instrumentation, and procedures (Frequency range of 4 MHz to 10 GHz)*. IEC/IEEE 62209-1528:2020, Oct. 2020.

[23] *IEEE Recommended Practice for Determining the Peak Spatial-Average Specific Absorption Rate (SAR) in the Human Head from Wireless Communications Devices: Measurement Techniques*. IEEE P1528/D6, March 2013.

[24] "Guidelines for limiting exposure to time-varying electric, magnetic, and electromagnetic fields (up to 300 GHz). International Commission on Non-Ionizing Radiation Protection.," *Health physics*, vol. 74 4, pp. 494–522, 1998.

[25] *IEEE Standard for Safety Levels with Respect to Human Exposure to Radio Frequency Electromagnetic Fields, 3 kHz to 300 GHz*. IEEE Std C95.1-1999, Apr. 1999.

[26] H. Moghnieh, M. Rammal, R. Barakeh, and E. Rachid, "Analysis of Human Head Interaction in Handset Antennas Using Ground Plane Corrugation," *IEEE Access*, vol. 12, pp. 151834–151845, 2024.

[27] *IEEE Standard for Safety Levels with Respect to Human Exposure to Electric, Magnetic, and Electromagnetic Fields, 0 Hz to 300 GHz*. IEEE PC95.1/D3.4, Sep. 2018.

[28] J. Bai, L. Wang, D. Wang, A. P. Duffy, and G. Zhang, "Validity Evaluation of the Uncertain EMC Simulation Results," *IEEE Trans. Electromagn. Compat.*, vol. 59, no. 3, pp. 797–804, Jun. 2017.

[29] G. Zhang, H. Sasse, L. Wang, and A. Duffy, "A Statistical Assessment of the Performance of FSV," *Applied Computational Electromagnetics Society Journal (ACES)*, vol. 28, no. 12, pp. 1179–1186, Sep. 2021.

[30] K. Ravindran and K. J. Vinoy, "A Reduced-Order PCE-Based Time-Domain Method for Large Uncertainties," *IEEE Trans. Antennas Propag.*, vol. 71, no. 6, pp. 5158–5165, Jun. 2023.